Analysis of the Thermal-Hydraulic Effects of a Plasma Disruption on the DTT TF Magnets

R. Bonifetto, *Member, IEEE*, M. De Bastiani, A. Di Zenobio, L. Muzzi, *Senior Member, IEEE*, S. Turtù, *Senior Member, IEEE*, R. Zanino, *Senior Member, IEEE*, and A. Zappatore, *Associate Member, IEEE*

***Abstract*—The Divertor Tokamak Test (DTT) facility, a fully superconducting nuclear fusion reactor being built in Italy, will contribute to address the power exhaust problem in EU DEMO perspective. A lot of flexibility of operation will be demanded to the machine, which should be capable to tackle also severe transients such as plasma disruptions. In this work, the 4C thermal-hydraulic code is used to compute the temperature margin during a plasma disruption, using as input the heat generated into the Toroidal Field coil casing and transferred to the winding pack, and the possibility that this leads to a quench of the magnet is studied. The results of the analysis will give important feedbacks for the design of the quench protection system, e.g., avoiding to trigger a fast current discharge right after the disruption, as well as for the machine operation, e.g., assessing the required re-cooling time of the magnets after a disruption.**

***Index Terms*—DTT, nuclear fusion, plasma disruptions, superconducting magnets, thermal-hydraulic modeling.**

I. Introduction

THE power exhaust represents a major challenge for the EUropean fusion reactor DEMOnstrator [1], asking for a new, robust design of the divertor, beyond the solution currently pursued for ITER [2]. For this reason, the construction of a satellite fusion experiment, the Divertor Tokamak Test (DTT) facility [3], focused on this subject, is being executed in Italy. This compact tokamak, which must be very flexible in terms of plasma configurations, will test several DEMO-relevant divertor solutions [4]–[6].

The DTT superconducting magnet system includes 18 Toroidal Field (TF) magnets, the Central Solenoid (CS) made of 6 modules and 6 Poloidal Field (PF) coils [7]. All of them are cooled by forced-flow supercritical helium at $\sim$6 bar and $\sim$4.5 K. In the case of a plasma disruption (PD), the fast decay of the plasma current (5.5 MA in reference scenario) causes a magnetic field variation, inducing on the one hand a sudden variation of the current in the PF and CS coils, and on the other hand AC losses in the conductors and eddy currents in the bulky steel structures (casing) of the TF coils. The latter causes a heat deposition that could erode the available temperature margin, up to the initiation of a quench in the worst case, thus requiring then a fast discharge (FD) of the coil current.

The 4C code [8], already used to analyze the pulsed plasma operation of the DTT TF magnets [9], [10] and of the CS and PF coils [11], is applied here to simulate the thermal-hydraulic effects of a plasma disruption on a DTT TF coil, similarly to what was already done for the ITER TF coils in [12]. The updates to the model presented in [10] are described first. Then the simulation setup is reported, and finally the simulation results are shown.

II. 4C Model of TF Magnet and Cryogenic Circuit

The DTT TF magnet system is composed by 18 identical coils [7]; both their winding pack (WP) and their casing are cooled (in parallel) with supercritical He (SHe) supplied by a single cryogenic circuit.

Due to the expected perfect toroidal symmetry of both the 18 coils and the thermal load applied in the transients at hand, a single TF magnet is modelled here, suitably downscaling the volume (cross section) of the cryolines.

A. TF Magnet

The geometry of the rectangular Cable-in-Conduit Conductors (CICCs), without low-impedance channel and equipped with Nb_3Sn strands, has been slightly updated with respect to that reported in [10], and is shown in Fig. 1(a). In the 4C model, the critical current scaling is taken from [14], with the parameters given in [10], except for the $C_0 = 89010$ A·T/mm^2 (slightly increased to account for the recent adoption of a strand showing better performance). The applied strain is assumed to be -0.65%. For the calculation of the friction factor, the modified Darcy-Forchheimer friction factor correlation for flow in porous media [15] is adopted.

Also the WP, composed of 5 double-pancakes (DPs), has been modified with respect to [10]: as reported in Fig. 1(b), the side pancakes feature now 6 turns instead of 4. A throttling valve is included at the outlet of those shorter pancakes, aiming at increasing their pressure drop to equalize the mass flow rate in each of the 10 pancakes. The inter-turn and inter-pancake thermal coupling is modelled as in [10], accounting for the thermal resistance (increased by a factor 5 to account for the multi-layer nature of the insulation, as observed from experimental data collected from JT-60SA central solenoid [16], KSTAR PF coils [17] and ITER CS modules [18]) of the 1 mm turn and 0.5 mm DP insulation. In principle this approach is suitable in a steady or quasi-steady condition. However, the same approach (less demanding in terms of computational cost than a detailed model

Manuscript received 7 December 2021; revised 17 February 2022; accepted 7 April 2022. Date of publication 12 April 2022; date of current version 14 July 2022. *(Corresponding author: Roberto Bonifetto.)*

R. Bonifetto, M. De Bastiani, R. Zanino, and A. Zappatore are with the NEMO Group, Dipartimento Energia, Politecnico di Torino, 10124 Torino, Italy (e-mail: roberto.bonifetto@polito.it; marco.debastiani@polito.it; roberto.zanino@polito.it; andrea.zappatore@polito.it).

A. Di Zenobio, L. Muzzi, and S. Turtù are with ENEA, Superconductivity Section, C.R. Frascati, 00044 Frascati, Italy.

Color versions of one or more figures in this article are available at https://doi.org/10.1109/TASC.2022.3166869.

Digital Object Identifier 10.1109/TASC.2022.3166869

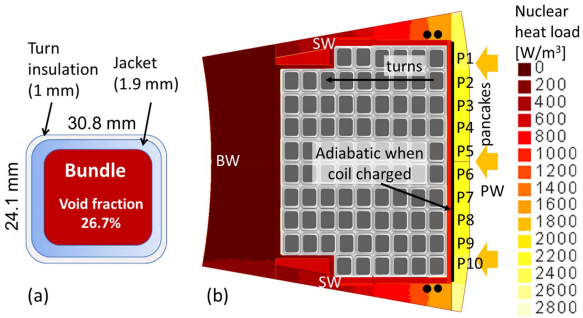

Fig. 1. (a) Cross section of the DTT TF conductor. (b) Radial-toroidal equatorial inboard cross section of the casing. The 2D color map shows the distribution of the nuclear heat load [13]; the orange arrows indicate the sides experiencing radiative heat load from the thermal shield. The location of the 4 casing cooling channels is shown by the black circles, while the black segment indicates the side of the WP considered adiabatic with respect to the casing when the coil is charged. The numbering of the pancakes adopted in this work is also shown. (PW = plasma wall, SW = side wall, BW = back wall).

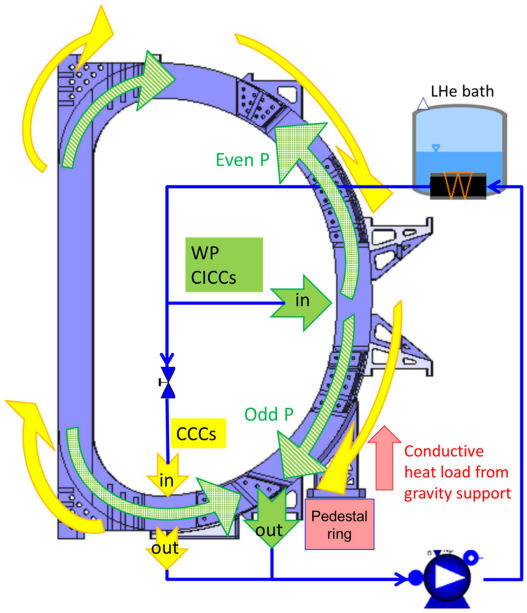

Fig. 2. Schematic view of the cooling of a DTT TF coil, showing the SHe cooling circuit, the inlets/outlets and the flow directions in both WP and casing cooling channels (green and yellow, respectively).

of the heat diffusion through the insulation) has been adopted and successfully validated on experimental data from a similar coil during fast current discharges. This can be understood considering that in such a transient the power is distributed, although with some spatial gradient, in the whole winding pack, contributing to reduce the effect of thermal gradients within the insulation. The thermal capacity of the insulation is in any case accounted for in the model.

The common inlet of each DP, shown in Fig. 2 to be placed on the inner coil surface, is now located at the equatorial outboard section, and results in a turn-by-turn counter-current SHe flow in adjacent pancakes (accounted for in the model), with all the 10 pancakes cooled in parallel; the outlets, joints and terminations (at the coil external radius) are located at the bottom. The latter is also the location of the inlets and outlets of the four parallel casing cooling channels (CCCs): each of them is a one-turn path, cooling first the inboard and then the outboard side of the casing.

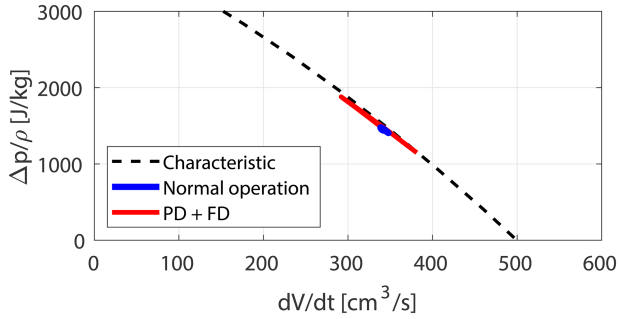

Fig. 3. Characteristic of the cold circulator adopted in the cryogenic circuit model. The operating point trajectories during normal operation (blue) and during a PD followed by an FD (red) are also reported.

They are hydraulically in parallel to the WP channels (Fig. 2); their location in the casing, close to the first turns of the side pancakes as shown in Fig. 1(b), is the same as in [10].

The bulky stainless-steel casing is poloidally discretized into 16 radial-toroidal 2D cuts (Fig. 1(b) shows the inboard equatorial one), following the discretization used to compute the nuclear heat load [13]. On each cut, the thermal conduction problem is solved, thermally coupled to the 1 mm thick stainless-steel pipe of the CCCs through 1 mm of epoxy resin impregnation; the small gap between the pipe and the casing is indeed assumed to be filled by a material (epoxy) with a thermal conductivity ~5 times lower than that of the metal (steel) used to weld the pipes to the casing: as the welding of such a small pipe should cover at least $^1/_4$ of the total perimeter, this should provide a conservative estimation of the coupling between the pipe and the casing. The investigation of other, more realistic options for the attachment of the CCCs to the casing is ongoing and will be presented elsewhere.

The casing is also thermally coupled to the WP through the 6 mm thick ground insulation, except on the plasma side: there, due to the Lorentz forces pushing the WP outwards, the casing-WP interface is considered adiabatic when the coil is charged, while the thermal coupling between the two is increased to the nominal value proportionally to the current ramp-down during the FD.

B. Cryogenic Circuit

During a severe transient like a PD followed by a FD, the assumption of constant inlet and outlet thermal-hydraulic boundary conditions for the WP and the CCCs done in [10] does not hold any more. To avoid the need of boundary conditions, the external cryogenic cooling circuit is also modelled here, see Fig. 2. Two pipelines of 25 m length and 2 cm diameter (the latter value is obtained scaling down the real, larger pipe area to consider that a single TF coil out of 18 is modelled here, preserving the SHe transit time) supply He at ~5 bar to the magnet. The CCC branch also contains a throttling valve to reduce the flow in the CCCs, having a much lower impedance than the CICCs, so that each pancake (and each CCC) carries ~2.5 g/s of He. A cold circulator provides ~2 bar nominal pressure head and a total SHe mass flow rate of ~35 g/s (for each TF coil), with the realistic (parabolic) characteristic shown in Fig. 3. Finally, the ideal heat transfer to a LHe bath at 4.55 K (to include possible radiative heat loads on the cryolines, with respect to the target 4.5 K temperature) is modelled, at the circulator outlet.

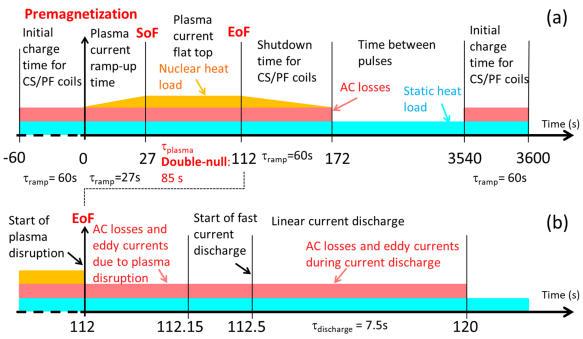

Fig. 4. (a) DTT reference Double-Null plasma scenario, including colored bands indicating the time intervals during which the heat deposition from AC losses, nuclear and static heat load takes place (the height of the band is not related to the value of the respective heat load). (b) Evolution of the plasma disruption initiated at EoB of the periodic plasma pulse. The time axis is not to scale. (SoF = start of plasma current flat-top, EoF = end of plasma current flat-top).

The safety valves (SVs) and the related quench lines present in the TF cooling circuit are neglected at present: if the SV opening set point (currently not defined yet) is overcome during the transient, this will result in an overestimation of the circuit pressurization that can occur in case of an accident where the SV would be stuck closed.

III. Simulation Setup

To assess the thermal-hydraulic effects of a PD with FD induced in the worst (although realistic) conditions, i.e., when the minimum temperature margin ($\Delta T_{\text{marg}}^{\text{min}}$) in the coil is reached during normal operation, the simulation of a series of standard plasma pulses is performed.

A. Plasma-Pulsed Operation

The scenario considered here (Double-Null, DN), presented in [11], with the evolution of the resulting heat loads on the magnets, is reported in Fig. 4(a): besides the nuclear heat load (the *pessimistic* case C in [10], i.e., with no neutron shield), resulting in a heat deposition of 820 kJ/cycle in the WP and 850 kJ/cycle in the casing, here also the following additional heat loads are considered:

- Static radiative, from the thermal shield (TS) conservatively assumed to be at 100 K (the foreseen outlet temperature of the TS cooling), considering an emissivity of 0.15 and 1 for the TS and the TF, respectively [3]; this heat load is applied to all the surfaces of the outboard leg and the plasma-facing surface of the inboard leg (see the orange arrows in Fig. 1(b)), as the other sides are either in contact with or facing other magnets at ∼4.5 K. The resulting radiative heat load is computed to be ∼20 W for each coil.
- Static conductive heat load from the gravity support, estimated to be ∼30 W for each TF coil.
- AC losses in the conductor due to the operation of the pulsed coils, neglected in [10]. The magnetic field (and its variation) within the TF conductors is computed at each instant of the scenario from the superposition of the magnetic field generated by all other coils (and the plasma), according to their transport current, as explained in Section 3.2 of [11]. The model described in [19], based on the single coupling time constant nτ (250 ms) with a saturation depending on the speed of the magnetic field variation, the characteristic time constant and the penetration field, is used to compute the power generated by AC coupling losses; for the hysteresis losses, the effective filament diameter of 15 μm is used. As a result, the peak power deposited in the WP by AC losses is ∼0.6 kW, and the energy deposited ∼40 kJ/cycle.

The static heat load from the PF supports is neglected here because, even though the static (radiative) heat load on the 6 PF coils is ∼320 W in total [11] (i.e., less than 20 W if considered to be equally split on all TF coils), it is assumed to be evacuated by the SHe cooling the PF magnets. The static heat load from the CS is considered negligible because the CS is mechanically supported by the TF coil casing and is almost completely facing cold surfaces at 4.5 K. The eddy currents induced in the casing by CS and PF during the normal operation are also neglected.

The effective magnetic field on the conductor cross section is computed and used to evaluate the $\Delta T_{\text{marg}}^{\text{min}}$.

The additional, above-mentioned heat loads tend to reduce the temperature margin, with respect to what computed in the past [10], as well as the introduction of the circuit model, because the latter properly accounts (also at the coil boundaries) for the reduction of the mass flow rate of fresh He at the WP inlet (and increase at the outlet) due to the He expansion and pressurization (up to ∼1 bar, not shown) in the WP during the plasma pulse, caused by the nuclear heat deposition (see Fig. 5(a)). On the other hand, the improved performance of the strands and the increase of the circulator pressure head to 2 bar, should both mitigate the $\Delta T_{\text{marg}}^{\text{min}}$ reduction: the results computed in each pancake at the periodic plasma pulse are reported in Fig. 5(b). The requirement of $\Delta T_{\text{marg}}^{\text{min}} \geq 1.4$ K is not strictly fulfilled, but at this stage the 0.1 K criterion exceedance is acceptable considering the conservative assumptions made in the present analysis. In particular, for the nuclear heat load a safety factor of 1.5 has been considered, and the most pessimistic DN scenario has been simulated even though it is not the reference one and features a plasma duration ∼40% and ∼50% longer than the baseline Single-Null and X-Divertor scenarios, respectively; a realistic analysis neglecting at least one of these two conservative assumptions would result in a minimum temperature margin ∼0.15 K higher, considering that the nuclear heat load erodes it by ∼0.5 K with respect to the 1.8 K computed during cold operation.

B. Plasma Disruption and Fast Current Discharge

The evolution of the $\Delta T_{\text{marg}}^{\text{min}}$ in the most critical pancake (P6) is shown in Fig. 5(c): as the $\Delta T_{\text{marg}}^{\text{min}}$ is reached at the EoF (∼112 s from the pre-magnetization), the PD is conservatively induced there, following the scenario reported in Fig. 4(b): the plasma current linearly decreases from 5.5 MA to 0 in less than 10 ms, inducing currents in the vacuum vessel (VV) conductive walls with a time constant <50 ms. The variation of the current in the plasma and in the VV, in turn, induces:

- a magnetic field variation in the WP [20], reported in Fig. 6(a) for the 8 different segments of the TF coil; this is used to compute the AC losses in the WP, with two different models for the coupling losses
  - case A: the single-time constant model without saturation regime described in [21], conservatively assuming the internal magnetic field to be equal to the external one (no screening effect, pessimistic option); see Fig. 6(b) for the evolution of the power deposition

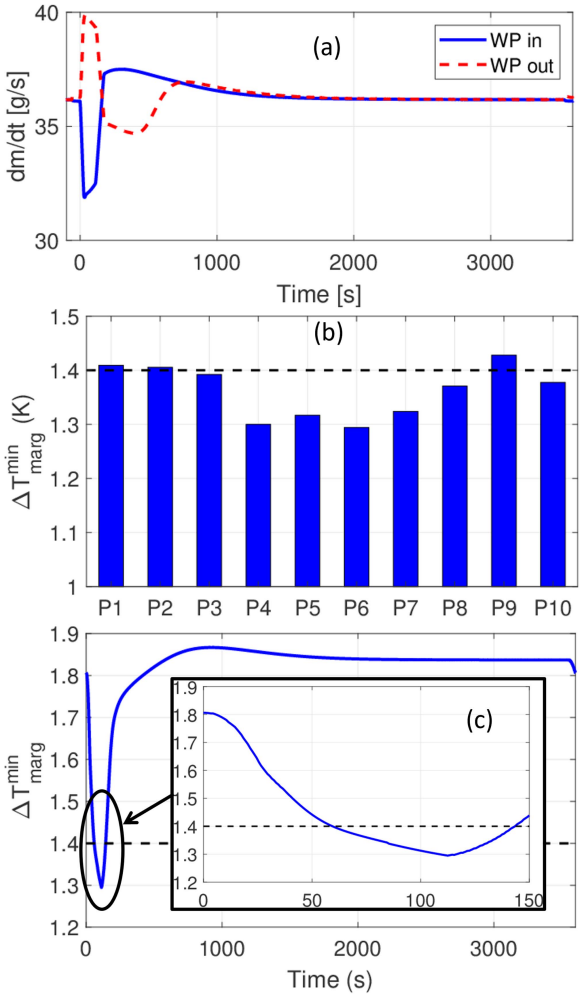

Fig. 5. Evolution of (a) the mass flow at coil (WP) boundaries; (b) $\Delta T^{\min}_{\text{marg}}$ computed in each pancake during the same transient; (c) evolution of the $\Delta T^{\min}_{\text{marg}}$ in P6 during a periodic plasma pulse (DN scenario). Time 0 s is set at premagnetization.

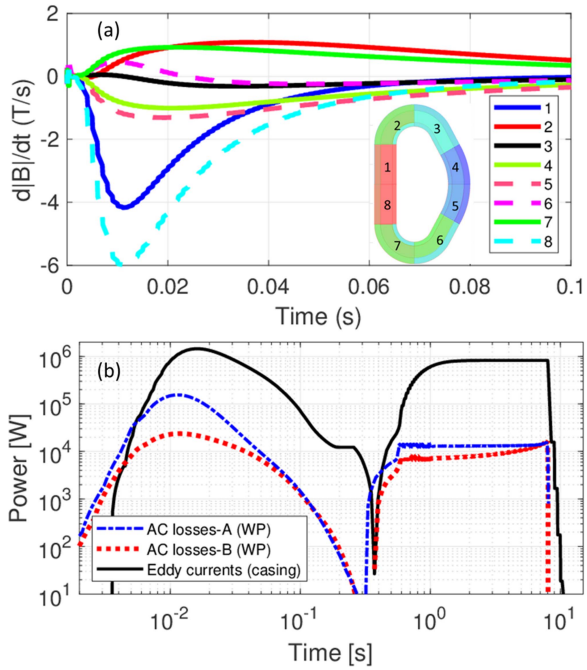

Fig. 6. (a) Evolution of the magnetic field variation at the different poloidal locations shown in the inset during the first 100 ms of the plasma disruption [20]. (b) Evolution of the power deposited by eddy currents in the casing during the plasma disruption and during the subsequent FD. The evolution of the power deposited by AC losses in the strands during the entire transient, computed by the 4C code, is also reported. Time 0 s is set at PD start.

TABLE I
ENERGY DEPOSITION IN ONE TF COIL DURING THE TRANSIENT

		Plasma disruption	Fast discharge
AC losses in WP	Case A	2.9 kJ	100 kJ
	Case B	860 J	77 kJ
Eddy currents in casing		51 kJ	6 MJ

- case B: the same model adopted for the normal operation analysis [19] (more realistic option), showing a peak power about one order of magnitude lower than case A; see Fig. 6(b) for the evolution of the power deposition
- eddy currents in the TF casing, see Fig. 6(b), causing a heat deposition on the ∼150 ms time-scale, computed with the model presented in [22]; the power is uniformly deposited in the entire casing.

During the PD, the TF coil current is supposed to be constant, as if it were not affected by the PD itself. This is not necessarily a conservative assumption, but no information on the current evolution is available for the time being.

After the PD, the possibility to also have a TF current FD is investigated. The FD is triggered automatically (without waiting for any quench detection) 0.5 s after the plasma disruption, see again Fig. 4(c). The FD consists in the controlled discharge of the 18 TF coil current with a linear ramp lasting 7.5 s [23]. This coil current variation, causing magnetic field variations, induces again AC losses (computed according to the two cases listed above for the PD) and eddy currents, computed with the model presented in [24]. The power deposition is different in each of the 16 poloidal cuts, but here it is assumed uniform within each of them. Note that in [24] it is shown that a linear FD induces eddy current power deposition in the casing ∼1/3 higher than the corresponding exponential dump (with time constant 2/3 of the linear ramp down time).

The entire heat load evolution is reported in Fig. 6(b), and the values of energy deposited are collected in Table I. Considering that the magnetic energy stored in the TF magnet system of DTT is ∼2 GJ, the energy deposited by eddy currents in the casing of the 18 coils during a linear FD is ∼5% of the magnetic energy. This value is intermediate between that of JT-60SA, where the energy deposited in the casing of all coils during an exponential FD with a time constant of 6.5 s is ∼1% [25] of the ∼1 GJ total energy stored in the TF magnets [26], and that of ITER (10% of the TF magnetic energy), which however features stainless-steel radial plates within the WP.

IV. RESULTS

The computed evolution of the $\Delta T^{\min}_{\text{marg}}$ in the TF coil during a PD without triggering a FD is reported in Fig. 7(a). For case A, the $\Delta T^{\min}_{\text{marg}}$ ∼0.4 K is reached in the first 10 ms, i.e., on the fast magnetic field variation (see Fig. 7(a) and its inset) inducing AC losses depositing heat directly in the WP. The over-conservative case in which the module of the magnetic field does not change in this phase (but still including the heat deposition due to

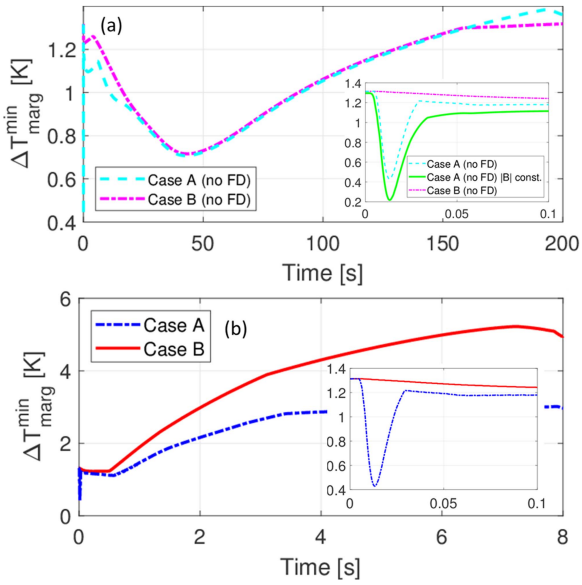

Fig. 7. Evolution of the computed $\Delta T_{\mathrm{marg}}^{\mathrm{min}}$ during the PD without FD (a) and with FD triggered 0.5 s after the disruption (b), with suitable zoom on the first 100 ms in the insets, for both AC loss models A and B. In (a) the conservative case where the magnetic field on the cable is not reduced during the PD is also reported. Time 0 s is set at PD start.

AC losses) is also reported, showing that even if the coil here would reach a lower margin (∼0.2 K), no current sharing is computed (see the inset of Fig. 7(a)). In case B, the $\Delta T_{\mathrm{marg}}^{\mathrm{min}}$ ∼0.7 K is reached ∼50 s after the PD, due to the conductor temperature increase caused by the heat deposited in the casing and transferred, across the ground insulation, to the WP. The time-scale of the heat conduction across the ground insulation is indeed ∼20 s at 10 K.

In the case with FD following the PD, see Fig. 7(b), the $\Delta T_{\mathrm{marg}}{}^{\mathrm{min}}$ in case A is unchanged as it is computed right after the PD. In case B, the $\Delta T_{\mathrm{marg}}^{\mathrm{min}}$ is instead >1 K, as during the current FD the temperature increase due to the AC losses and eddy currents is slower than the current sharing temperature (T_{CS}) increase due to the current ramp down. Note that after 8 s (following the PD start) the current in the coil is zero, so that since then it would be meaningless to argue about the $\Delta T_{\mathrm{marg}}^{\mathrm{min}}$.

The value of hot spot temperature in the conductor (and casing) for case B is reported in Fig. 8, for a PD followed or not by a FD. On the fast time-scale of the PD, it increases by ∼0.5 K (see Fig. 8(c)), but on one hand the hot spot is not located in the same position where the $\Delta T_{\mathrm{marg}}^{\mathrm{min}}$ is computed (see Fig. 9), and on the other hand the magnetic field reduces by ∼0.1 T (in the $\Delta T_{\mathrm{marg}}^{\mathrm{min}}$ location at the equatorial inboard, namely at ∼1/2 of the first turn length, i.e., ∼5 m from the inlet in Fig. 9), resulting in a significant T_{CS} increase. As a result, the $\Delta T_{\mathrm{marg}}^{\mathrm{min}}$ in case B is poorly affected by the PD. On the contrary, the hot spot temperature increase in case A during the PD is ∼0.7 K higher than in case A (see Fig. 8(c)), so that the temperature margin erosion is higher by almost the same amount (see Fig. 7(b)). In case A, indeed, due to the lack of a saturation model for the coupling losses, the heat deposition in the equatorial inboard region (where also the minimum T_{CS} is reached, being the peak magnetic field located there) is higher than in case B.

The evolution of the hot spot temperature on a longer time scale is also shown in Fig. 8(a) and (b) for both cases with PD not followed or followed by a FD, respectively: in the former case,

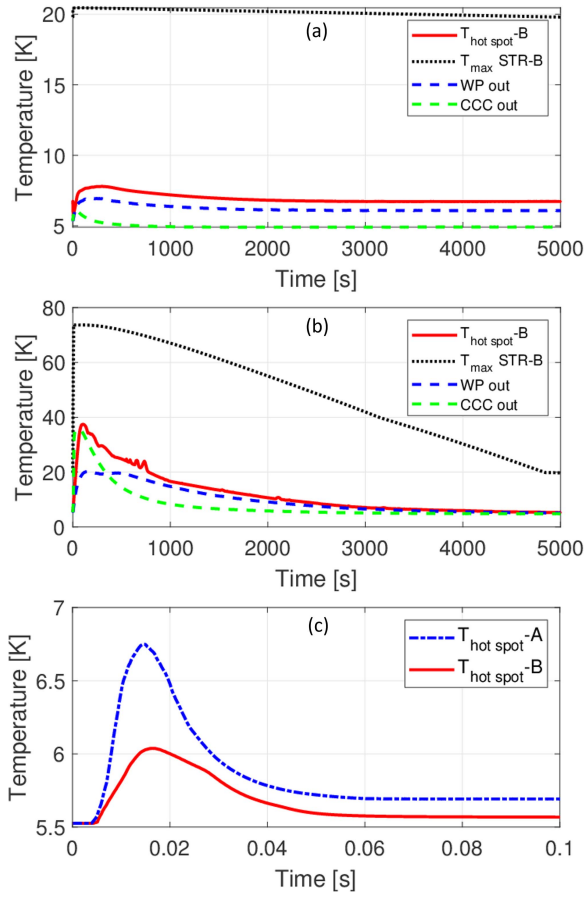

Fig. 8. Evolution of the computed temperature during the transient. Case B: hot-spot, inlet and outlet temperature in the WP, and maximum casing (STR) temperature during the PD (a) and PD followed by a FD (b). The hot-spot temperature in the WP for both cases A and B during the first 100 ms is also shown (c). Time 0 s is set at PD start.

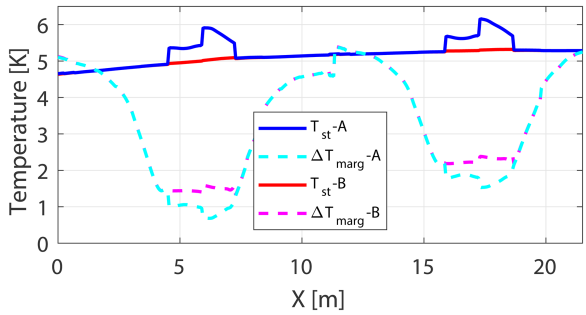

Fig. 9. Distribution of the strand temperature in the first two turns of P6 10 ms after the start of the PD, for both cases A and B. The $\Delta T_{\mathrm{marg}}^{\mathrm{min}}$ distribution is also reported. 0 m is set at the cooling path inlet, at the coil bore of the equatorial outboard segment.

its increase is limited to few kelvin, while in the latter it reaches a peak of ∼40 K, due to the heat deposited in the casing by eddy currents and conducted to the WP through the ground insulation, also considering that after the coil is discharged the plasma side of the WP is in perfect thermal contact with the casing. The casing temperature increases by ∼1 K during the PD (see again Fig. 8(a)), but its peak is ∼70 K at the end of the FD (Fig. 8(b)), due to the large heat deposited by eddy currents (∼6 MJ/coil), and it requires ∼1.5 h to be re-cooled to the operating value

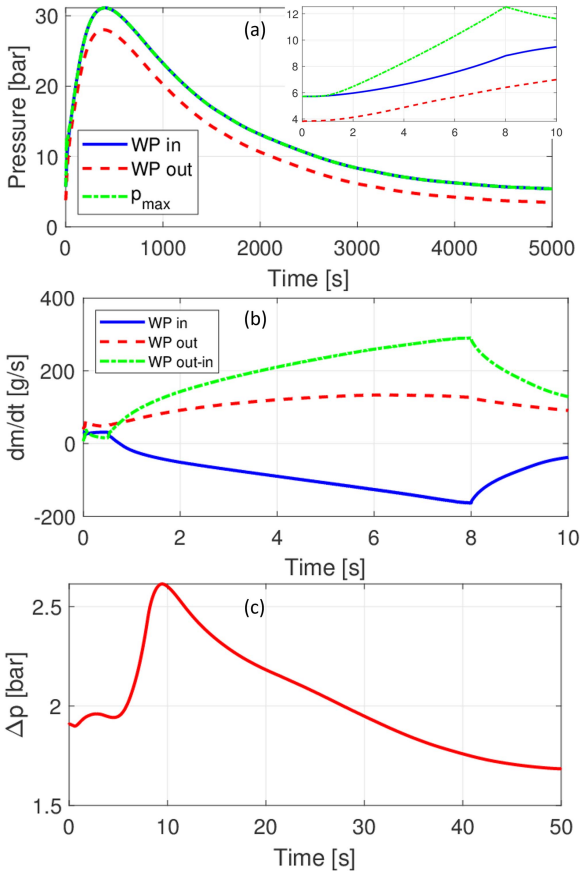

Fig. 10. Computed evolution of (a) the (maximum) pressure in the coil and at its boundaries during the PD followed by FD (a zoom on the first 10 s of the transient is reported in the inset); (b) the mass flow at coil (WP) boundaries during the first 10 s; (c) the pressure head across the cold circulator. Results for case B are shown. Time 0 s is set at PD start.

(showing a local maximum casing temperature of ∼20 K): even though the outlet temperature of the CCCs seems to recover the cold operation value in ∼0.5 h (also in view of the transit time in the CCCs, much shorter than in the WP, see below), being the peak casing temperature far away from the CCC location it needs much longer to be reduced to values typical of the cold operating conditions.

The re-cooling of the WP is instead faster, taking ∼1 h, as it can be seen by the stabilization of the temperature at the WP outlet (Fig. 8(b)). Note that, being the transit time of the He in the WP ∼500 s, the WP outlet temperature starts decreasing on that time-scale; on the contrary, being the transit time in the CCCs much shorter (∼30 s), the temperature at the CCC outlet starts decreasing much in advance.

The pressurization of the SHe circuit is shown in Fig. 10(a): it reaches values as high as ∼30 bar. Note however that, as stated in the description of the cryogenic circuit model, the opening of the SVs is conservatively not accounted for. This has also an impact on the estimated re-cooling time, which is a lower bound value as it does not consider the need to refill the cryogenic circuit with the SHe vented from the SVs.

During the FD the maximum pressure is located within the WP, as reported in the inset of Fig. 10(a), due to the strong heat deposition caused by AC losses and consequent He pressurization and expulsion at both inlet and outlet (see also Fig. 10(b)). No He expulsion at the inlet is instead computed during the PD, even though the difference between outlet and inlet mass flow rate reacts on the time-scale of the PD. During the re-cooling transient, as expected, the peak pressure in the WP is located at the inlet, as the normal flow direction is re-established. As for the temperature, also the pressure reaches the normal operating value ∼1.5 h after the PD start.

The pressure head across the cold circulator is also reported in Fig. 10(c). From the nominal value of ∼2 bar, it is computed to increase up to 2.6 bar. If this could be dangerous for the stability and mechanical resistance of the cold circulator shaft, it is worth considering a protection strategy, e.g., the temporary coil by-pass (through a suitable valve) during the FD with isolation of the coil (through control valves at its inlet and outlet), as done, e.g., for the ITER CS module tests in the final test facility [27], preventing the pressure wave to reach the cold circulator. The trajectory of its operating point both during the normal operation and the PD followed by a FD, reported in Fig. 3, shows indeed that in accidental conditions the pressure head can vary in a range as wide as 2/3 of its nominal value, with potential consequences on the stability of the circulator operation.

V. Conclusions and Perspective

The analysis of the thermal-hydraulic effects of a plasma disruption induced at the end of the plasma current flat-top, possibly followed by a fast current discharge on the DTT TF coils, has been carried out for the first time with the 4C code.

The model of one TF magnet has been updated to include its cryogenic circuit, suitably rescaled to fit the model of a single TF coil. The power deposition by eddy currents in the casing and AC losses in the winding pack (with two different models, one more pessimistic and the other more realistic) has been accounted for as main driver.

The most conservative AC loss model foresees a temperature margin reduction down to less than 0.5 K during the disruption, in view of the direct heat deposited in the conductors, but still avoiding the current sharing regime. This implies that there is no need to trigger a fast current discharge of the TF coils to prevent their quench during the disruption.

Even if a fast discharge is triggered by other signals, the analyses show that the temperature margin does not reduce further. However, the strong heat deposition during the current discharge causes a heating of the conductors and of the casing up to ∼40 K and ∼70 K, respectively, requiring at least ∼1.5 h to be re-cooled to operating conditions. The pressure head across the cold circulator increases by more than 25%, possibly requiring the adoption of suitable protection strategies. This confirms that, according to the inputs available so far for the analysis presented here, the fast discharge should not be foreseen after a plasma disruption.

In perspective, an assessment of the impact of input uncertainties ($n\tau$ time constant, eddy currents, …) is envisaged, as well as the implementation of the safety valves opening towards the quench lines. The 4C code is also going to be used to analyze the effects of a plasma disruption on the CS and PF coils.

References

[1] G. Federici *et al.*, "DEMO design activity in Europe: Progress and updates," *Fusion Eng. Des.*, vol. 136, pp. 729–741, 2018.

[2] A. J. H. Donné, G. Federici, X. Litaudon, and D. C. McDonald, "Scientific and technical challenges on the road towards fusion electricity," *J. Instrum.*, vol. 12, no. 10, 2017, Art. no. C10008, [Online]. Available: https://doi.org/10.1088/1748-0221/12/10/C10008

[3] R. Martone, R. Albanese, F. Crisanti, A. Pizzuto, and P. M. Eds, "DTT divertor tokamak test facility interim design report," ENEA, *Green Book*, Apr. 2019, Accessed: Dec. 7., 2021, [Online]. Available: https://www.dtt-project.it/downloads/DTT_IDR_2019_WEB.pdf

[4] G. M. Polli *et al.*, "DTT's role, characteristics & design status," in *Proc. IEEE 20th Mediterranean Electrotechnical Conf.*, 2020, pp. 640–645, doi: 10.1109/MELECON48756.2020.9140576.

[5] G. Mazzitelli *et al.*, "Role of Italian DTT in the power exhaust implementation strategy," *Fusion Eng. Des.*, vol. 146, pp. 932–936, 2019.

[6] R. Albanese *et al.*, "Design review for the Italian divertor tokamak test facility," *Fusion Eng. Des.*, vol. 146, pp. 194–197, 2019.

[7] A. Di Zenobio *et al.*, "DTT: A challenging framework for a sound superconducting magnets design," *IEEE Trans. Appl. Supercond.* vol. 32, no. 6, Sep. 2022, Art. no. 4201005, doi: 10.1109/TASC.2022.3153235.

[8] L. Savoldi Richard, F. Casella, B. Fiori, and R. Zanino, "The 4C code for the cryogenic circuit conductor and coil modeling in ITER," *Cryogenics*, vol. 50, pp. 167–176, 2010.

[9] A. Di Zenobio *et al.*, "DTT device: Conceptual design of the superconducting magnet system," *Fusion Eng. Des.*, vol. 122, pp. 299–312, Nov. 2017.

[10] R. Bonifetto, A. Di Zenobio, L. Muzzi, S. Turtu, R. Zanino, and A. Zappatore, "Thermal-hydraulic analysis of the DTT toroidal field magnets in DC operation," *IEEE Trans. Appl. Supercond.*, vol. 30, no. 4, Jun. 2020, Art. no. 4200605, doi: 10.1109/TASC.2020.2964517.

[11] R. Bonifetto, A. Di Zenobio, L. Muzzi, S. Turtù, R. Zanino, and A. Zappatore, "Thermal-hydraulic analysis of the DTT CS and PF pulsed coils performance during AC operation," *Fusion Eng. Des.*, vol. 173, 2021, Art. no. 112836, doi: 10.1016/j.fusengdes.2021.112836.

[12] L. Savoldi Richard, D. Bessette, R. Bonifetto, and R. Zanino, "Parametric analysis of the ITER TF fast discharge using the 4C code," *IEEE Trans. Appl. Supercond.*, vol. 22, no. 3, Jun. 2012, Art. no. 4704104, doi: 10.1109/TASC.2012.2188130.

[13] R. Villari *et al.*, "Nuclear design of divertor tokamak test (DTT) facility," *Fusion Eng. Des.*, vol. 155, 2020, Art. no. 111551, doi: 10.1016/j.fusengdes.2020.111551.

[14] L. Bottura and B. Bordini, "$J_c(B, T, \varepsilon)$ parameterization for the ITER Nb_3Sn production," *IEEE Trans. Appl. Supercond.*, vol. 19, no. 3, pp. 1521–1524, Jun. 2009.

[15] M. Lewandowska and M. Bagnasco, "Modified friction factor correlation for CICC's based on a porous media analogy," *Cryogenics*, vol. 51, pp. 541–545, 2011.

[16] R. Bonifetto, L. Savoldi, and R. Zanino, "Thermal-hydraulic analysis of the JT-60SA central solenoid operation," *IEEE Trans. Appl. Supercond.*, vol. 29, no. 5, Aug. 2019, Art. no. 4201005.

[17] L. Savoldi Richard *et al.*, "4C code analysis of thermal-hydraulic transients in the KSTAR PF1 superconducting coil," *Cryogenics*, vol. 53, Jan. 2013, pp. 37–44.

[18] A. Zappatore, R. Bonifetto, N. Martovetsky, and R. Zanino, "Development and validation of the 4C thermal-hydraulic model of the ITER central solenoid modules," submitted to Cryogenics, 2022.

[19] N. Pompeo and L. Muzzi, "The superconducting proposal for the CS magnet system of FAST: A preliminary analysis of the heat load due to AC losses," 2011, *arXiv*: 1101.5825.

[20] R. Albanese, R. Fresa, G. Rubinacci, and F. Villone, Consorzio CREATE, personal communication, Oct. 2019.

[21] M. N. Wilson, *Superconducting Magnets*. Oxford, U.K.: Clarendon, 1983.

[22] G. Messina, L. Morici, A. Di Zenobio, L. Muzzi, S. Turtù, and G. Ramogida, "Electromagnetic analysis of DTT poloidal field coils during an electrical transient," *IEEE Trans. Appl. Supercond.*, vol. 32, no. 6, Sep. 2022, Art. no. 4202905, doi: 10.1109/TASC.2022.3165477.

[23] C. R. Lopes *et al.*, "Design optimization for the quench protection of DTT's superconducting toroidal field magnets," *Fusion Eng. Des.*, vol. 172, 2021, Art. no. 112748, https://doi.org/10.1016/j.fusengdes.2021.112748.

[24] R. Bonifetto, M. De Bastiani, R. Zanino, and A. Zappatore, "3D-FOX - a 3D transient electromagnetic code for eddy currents computation in superconducting magnets structures: DTT TF fast current discharge analysis," to be submitted for publication.

[25] A. Louzguiti, Q. Le Coz, S. Nicollet, A. Torre, B. Turck, and L. Zani, "Modeling of AC losses and simulation of their impact on JT-60SA TF magnets during commissioning," *IEEE Trans. Appl. Supercond.*, vol. 31, no. 5, Aug. 2021, Art. no. 4200605, doi: 10.1109/TASC.2021.3051324.

[26] L. Novello *et al.*, "Analysis of maximum voltage transient of JT-60SA toroidal field coils in case of fast discharge," *IEEE Trans. Appl. Supercond.*, vol. 26, no. 2, Mar. 2016, Art. no. 4700507, doi: 10.1109/TASC.2016.2521321.

[27] M. Breschi *et al.*, "AC losses in the first ITER CS module tests: Experimental results and comparison to analytical models," *IEEE Trans. Appl. Supercond.*, vol. 31, no. 5, Aug. 2021, Art. no. 5900905, doi: 10.1109/TASC.2021.3061950.